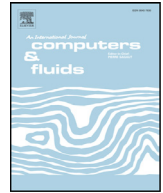




ELSEVIER

Contents lists available at ScienceDirect

Computers and Fluids

journal homepage: [www.elsevier.com/locate/complfluid](http://www.elsevier.com/locate/complfluid)

# Accuracy improvement of the immersed boundary–lattice Boltzmann coupling scheme by iterative force correction



Chunze Zhang<sup>a</sup>, Yongguang Cheng<sup>a,\*</sup>, Luoding Zhu<sup>b</sup>, Jiayang Wu<sup>a</sup>

<sup>a</sup> State Key Laboratory of Water Resources and Hydropower Engineering Science, Wuhan University, Wuhan 430072, PR China

<sup>b</sup> Department of Mathematical Sciences, Indiana University–Purdue University Indianapolis, Indianapolis, IN 46202, United States

## ARTICLE INFO

### Article history:

Received 20 December 2014

Revised 14 March 2015

Accepted 27 March 2015

Available online 3 April 2015

### Keywords:

Immersed boundary method

Lattice Boltzmann method

Fluid–structure interaction

Non-slip boundary condition

External forcing term

Mechanical heart valves

Iterative method

## ABSTRACT

The non-slip boundary condition at solid walls cannot be accurately achieved by the conventional immersed boundary–lattice Boltzmann (IB–LB) coupling schemes due to insufficient interpolation accuracy. To solve this problem, an iterative force correction procedure for the IB–LB coupling scheme is proposed. Cheng's external forcing term in the LB equation is selected to properly incorporate the present and the next time step effects. The unknown IB force and the corresponding force on fluid at the next time step are calculated by iterative correction, based on the known immersed boundary speed, flow velocity, and the relationship between the IB speed and the IB force. Instead of the Dirac delta function, the Lagrange interpolation polynomial is used to obtain the IB speed from nearby fluid velocity. Typical cases, including the flow around a circular cylinder, shearing flow near a non-slip wall, and circular Couette flow between two inversely rotating cylinders, are simulated to verify and validate the method. It is shown that the present method guarantees the non-slip boundary condition and maintain the overall first-order spatial convergence rate of the conventional immersed boundary method (IBM). The accuracy improvement is obvious for both stationary and moving solid boundaries in both viscous flows and strong shearing flows. To demonstrate application possibility, a mechanical heart valve flow is also simulated, and better agreements with experimental data are achieved compared to those by commercial software.

© 2015 Elsevier B.V. All rights reserved.

## 1. Introduction

The immersed boundary (IB) method was first proposed by Peskin in 1970s to simulate blood flows in the human heart [1]. This method uses a fixed Eulerian mesh to simulate the flow field, and a set of Lagrangian points to represent the boundary immersed in the fluid. The interaction between the fluid and the immersed boundary is implemented by a discrete Dirac delta function, which spreads the force of the deformable elastic boundary to the nearby fluid grid nodes and interpolates the boundary velocity from the local flow velocity to update the boundary position. Since Peskin's pioneering work, the IB method has been widely used to study a variety of fluid–structure interaction (FSI) problems, including blood flow in the human heart [2], flows through prosthetic cardiac valves [3], swimming of bacterial organisms and aquatic animals [4,5] aggregation of platelets [6], deformation of three-dimensional capsules [7,8], filament flapping [9,10], and parachute opening dynamics [11].

The lattice Boltzmann (LB) method is an alternative simulation technique for complex fluid systems [12–14]. Its easy implementation, intrinsic parallelism, and good suitability for numerous fluid flow problems have been demonstrated by many works [15–18]. Like the IB method, the standard LB method works on a regular grid. Due to this common feature, coupling these two methods for efficient simulation of FSI problems is possible. Researchers have made many efforts in improving and applying the IB–LB coupling schemes in recent years. Zhang et al. [6] proposed an IB–LB coupling scheme to investigate aggregation of red blood cells. Cheng and Zhang [19] improved the forcing introducing method and analyzed the mitral valve flow. Tian et al. [20] presented a modified penalty IB–LB scheme to simulate the flapping of multiple elastic filaments. Krüger et al. [8] used the finite element LB model in the scheme and simulated the deformation of an initially spherical capsule freely suspended in simple shear flow. Hao and Zhu [21] proposed an implicit IB schemes to simulate a 3D viscous flow past deformable sheets and flags. In the above works, the boundaries were flexible and the boundary force was evaluated from the boundary configuration following the physical law. On the other hand, several other IB–LB coupling schemes have been proposed to simulate moving rigid boundaries. They used different

\* Corresponding author.

E-mail addresses: [ygcheng@whu.edu.cn](mailto:ygcheng@whu.edu.cn) (Y. Cheng), [lzhu@math.iupui.edu](mailto:lzhu@math.iupui.edu) (L. Zhu).

approaches to calculate the IB force that is spread to the fluid nodes through the Dirac delta function. Feng and Michaelides [22] proposed a penalty method that allows the solid particles to be slightly deformed and assumed a linear spring to restore the IB points back to their target location. Niu et al. [23] calculated the IB force by the momentum exchange of the particle distributions of LB model at boundary. Dupuis et al. [24] introduced a direct forcing IB method, in which the IB force was obtained by comparing the computed IB speed with the desired reference speed without applying the IB force. However, the non-slip boundary condition cannot be exactly guaranteed by the above mentioned methods. Some researchers have made efforts to remedy this problem. For example, Cheng et al. [25,27] assigns the zero velocity to the Eulerian points inside of the stationary solid body at every evolutionary time step. This artifice can enhance the non-slip boundary condition, but is not convenient in simulating complex moving bodies. Later, Wu and Shu [26] develops an implicit velocity correction-based IB–LB scheme by using Guo’s external forcing term [28]. Although the scheme can well enhance the non-slip boundary condition by correcting IB speed, it needs to solve a large banded matrix  $((2N_b)^2$  in two dimensions and  $(3N_b)^2$  in three dimensions, where  $N_b$  is the number of IB points). The consumed memory and computing time increase significantly as  $N$  increases, which imposes a limitation on the Lagrangian grid density of IB discretization. In order to improve the accuracy at boundary walls without significantly increasing computing cost, a new iterative force correction IB–LB coupling scheme is introduced in this paper. It is based on the LB equation with the external forcing term proposed by Cheng and Li [29]. The external forcing term (see Section 2), which consists of the present and the next time step effects, can maintain the second-order overall spatial accuracy, and does not have to modify the formulae for computing macroscopic fluid flow velocity. The computing cost of the force correction does not increase significantly because only the fluid flow nodes within the IB layer (the influence range of boundary force) are involved in the iteration.

The paper is organized as follows. Section 2 briefly describes the related existing IB–LB coupling schemes. Section 3 introduces the new iterative force correction scheme. In Section 4, the accuracy of the proposed scheme is verified by typical problems. In Section 5, the mechanical heart valve flow is simulated and compared with experimental data. Section 6 concludes the paper.

## 2. Existing immersed boundary–lattice Boltzmann coupling schemes

### 2.1. Immersed boundary method

In the IB method, the flow field is described on a fixed Eulerian mesh  $\Omega_f$ , and the IB is represented by sets of Lagrangian points  $\Gamma_b$ . The formulation may be expressed as follows:

$$\frac{\partial \rho}{\partial t} + \nabla \cdot (\rho \mathbf{u}) = 0, \tag{1}$$

$$\frac{\partial (\rho \mathbf{u})}{\partial t} + \nabla \cdot (\rho \mathbf{u} \mathbf{u}) = -\nabla p + \nu \nabla \cdot [\rho (\nabla \mathbf{u} + (\nabla \mathbf{u})^T)] + \mathbf{f}, \tag{2}$$

$$\frac{\partial \mathbf{X}_i(s,t)}{\partial t} = \mathbf{U}(\mathbf{X}_i,t) = \int_{\Omega_f} \mathbf{u}(\mathbf{x},t) \delta(\mathbf{x} - \mathbf{X}_i(s,t)) d\mathbf{x}, \tag{3}$$

$$\mathbf{f}(\mathbf{x},t) = \int_{\Gamma_b} \mathbf{F}(s,t) \delta(\mathbf{x} - \mathbf{X}(s,t)) ds, \tag{4}$$

$$\mathbf{F}(s,t) = S_f \mathbf{X}(s,t), \tag{5}$$

where  $\mathbf{x}$ ,  $p$ ,  $\mathbf{u}$  and  $\mathbf{f}$  are the Eulerian spatial coordinate, flow pressure, fluid velocity, and external force density, respectively;  $\mathbf{X}_i$ ,  $\mathbf{F}$  and  $\mathbf{U}$  are

the Lagrangian IB position, IB force density, and IB moving speed, respectively;  $S_f$  is the IB force generation operator;  $\delta(r)$  is the delta function which may be written as

$$\delta_h(x,y) = h^{-2} \phi\left(\frac{x}{h}\right) \phi\left(\frac{y}{h}\right), \tag{6}$$

in which  $h$  is the mesh spacing, and  $\phi(r)$  is normally chosen as

$$\phi(r) = \begin{cases} \frac{1}{8} \left( 3 - 2|r| + \sqrt{1 + 4|r| - 4|r|^2} \right) & 0 \leq |r| < 1, \\ \frac{1}{8} \left( 5 - 2|r| + \sqrt{-7 + 12|r| - 4|r|^2} \right) & 1 \leq |r| < 2, \\ 0 & |r| \geq 2. \end{cases} \tag{7}$$

Eqs. (1) and (2) are the N–S equations with external force  $\mathbf{f}$  in Eulerian form for the fluid flow in domain  $\Omega_f$ , while Eqs. (3)–(5) are the dynamic equations in Lagrangian form for the boundary  $\Gamma_b$ . Eqs. (3) and (4) describe the interaction between the IB and fluid flow. The former imposes the flow velocity on the boundary to obtain IB velocity  $\mathbf{U}$  and the latter spreads the Lagrangian IB force to the fluid to obtain the Eulerian force. Eq. (5) is the constitutive equation that determines IB force based on the boundary configuration, in which function  $S_f$  satisfies a generalized Hooke’s law if the boundary is elastic.

### 2.2. Lattice Boltzmann method for fluid flow

#### 2.2.1. Basic formulation of the LB model with multi-relaxation-time collision

In this work, the LB model with multi-relaxation-time (MRT) collision operator is used for the fluid flow simulation. The most common two-dimensional LB model is the one using a square lattice with nine discrete velocity directions (denoted as D2Q9). The MRT-LB model with external forcing may be written as

$$f_\alpha(\mathbf{x} + \mathbf{e}_\alpha \delta t, t + \delta t) - f_\alpha(\mathbf{x}, t) = -M^{-1} \hat{S} [m_\alpha(\mathbf{x}, t) - m_\alpha^{eq}(\mathbf{x}, t)] + \delta t F_\alpha, \tag{8}$$

where  $\{f_\alpha(\mathbf{x}, t) : \alpha = 0, 1, \dots, 8\}$  are the discrete distribution functions at position  $\mathbf{x}$  and time  $t$ ;  $\{F_\alpha : \alpha = 0, 1, \dots, 8\}$  are the external forcing term which play a key role in the new IB–LB coupling scheme and will be discussed elaborately in Section 2.2.2;  $\{m_\alpha(\mathbf{x}, t) : \alpha = 0, 1, \dots, 8\}$  are the moments of the distribution functions and may be expressed as  $m = (\rho, e, \varepsilon, j_x, q_x, j_y, q_y, p_{xx}, p_{xy})^T$ . The physical meanings of the above moments can be found in literature [30]. The relation between  $m$  and distribution function  $f$  may be expressed as  $m = Mf$ , where  $M$  is the transformation matrix [30].  $m^{eq}$  is the equilibrium moments, which may be expressed as

$$m^{eq} = \rho \left( 1, -2 + 3u^2, 1 - 3u^2, u_x, -u_x, u_y, -u_y, u_x^2 - u_y^2, u_x u_y \right)^T.$$

The diagonal collision matrix  $\hat{S}$  may be given by

$$\hat{S} = \text{diag}(s_\rho, s_e, s_\varepsilon, s_\chi, s_q, s_\chi, s_q, s_\nu, s_\nu).$$

The fluid density  $\rho$  and flow velocity  $\mathbf{u}$  are defined as

$$\rho = \sum_\alpha f_\alpha, \quad \rho \mathbf{u} = \sum_\alpha \mathbf{e}_\alpha f_\alpha. \tag{9}$$

#### 2.2.2. Cheng’s approach for introducing external force into the LB model

The external forcing term of the LB model play a significant role in accuracy and stability of simulations. Here the approach proposed by Cheng and Li [29] is adopted and it is the basis of the new IB–LB coupling scheme (the derivation can be found in

**Section 3**). The method can handle time and space dependent body forces or other source terms and need not to modify the calculation formula of velocity (Eq. (9)). Both theoretical analysis and numerical simulation of typical examples have shown that a second-order accuracy can be achieved within incompressible limit [29].

Assuming that  $A$  is the source term in the continuity equation and  $\mathbf{B}$  is the external forcing term in the momentum equations, Cheng's forcing term in Eq. (8) may be written as [29]

$$F_\alpha = \frac{1}{2} [g_\alpha(\mathbf{x} + \mathbf{e}_\alpha \delta t, t + \delta t) + g_\alpha(\mathbf{x}, t)], \quad (10)$$

$$g_\alpha = w_\alpha \{A + 3\mathbf{B} \cdot [(\mathbf{e}_\alpha - \mathbf{u}) + 3(\mathbf{e}_\alpha \cdot \mathbf{u})\mathbf{e}_\alpha]\}, \quad (11)$$

where  $w_\alpha$  is the weighting factor, which takes  $w_0 = 4/9$ ,  $w_{1-4} = 1/9$  and  $w_{5-8} = 1/36$  for D2Q9 model. For Eqs. (1) and (2) here, we may let  $A = 0$  and  $\mathbf{B} = \mathbf{f}$ .

### 2.3. Four related existing IB-LB coupling schemes

Four existing IB-LB coupling schemes, the penalty method [22], direct forcing method [24], momentum exchange method [23], and velocity correction method [26] will be used to compare with the present scheme in this paper. The first three are explicit schemes. Thus, the interpolation error is fixed and the simulated velocity does not satisfy exactly the non-slip boundary condition at walls. This leads to penetration of fluid into the solid body. The last velocity correction method is an implicit scheme, in which the boundary force is computed implicitly and the non-slip boundary condition is enforced at the IB points. However, because a large banded matrix must be calculated during the solving procedures, the computer memory consumption and computing time will increase significantly with the number of IB discrete points increasing. The four schemes will be briefly discussed in this section.

#### 2.3.1. Penalty method

To model the interaction of the fluid and the rigid body, Feng and Michaelides [22] used the penalty method to compute the IB force. This method assumes that a IB point should be at its reference position  $\mathbf{X}_j^r$  although its actual position is  $\mathbf{X}_j^t$  because the boundary is slightly deformed by the fluid. If the reference point and the IB point are not coincided at the same position, the displacement  $\xi_j = \mathbf{X}_j^t - \mathbf{X}_j^r$  will generate a restoration force  $\mathbf{F}_j$  that tends to restore the boundary point back to the reference point. This can be modeled by a linear spring relation:

$$\mathbf{F}_j = -\kappa \xi_j, \quad (12)$$

where  $\kappa$  is the spring constant, and it can be empirically determined by users.

#### 2.3.2. Direct forcing method

To eliminate the artificial  $\kappa$ , Dupuis et al. [24] introduced the direct forcing method. It is assumed that Eq. (2) is also valid at the IB points, therefore Eq. (2) can be rewritten as

$$\frac{\partial \mathbf{u}}{\partial t} = \frac{\mathbf{u}^d(\mathbf{x}, t + \delta t) - \mathbf{u}(\mathbf{x}, t)}{\delta t} = \text{RHS} + \mathbf{f}(\mathbf{x}, t), \quad (13)$$

where  $\mathbf{u}^d$  is the desired reference velocity (equal to the IB speed),  $\text{RHS} = -\nabla \cdot (\mathbf{u}\mathbf{u}) - \nabla p + \nu \nabla \cdot [(\nabla \mathbf{u} + (\nabla \mathbf{u})^T)]$ . With external force density neglected, Eq. (2) can be rewritten as

$$\frac{\mathbf{u}^*(\mathbf{x}, t + \delta t) - \mathbf{u}(\mathbf{x}, t)}{\delta t} = \text{RHS}, \quad (14)$$

where  $\mathbf{u}^*$  is the flow velocity at time  $t + \delta t$  without forcing term. Subtracting Eq. (14) from (13) yields an expression for the fluid flow force at IB points

$$\mathbf{f}(\mathbf{x}, t) = \frac{\mathbf{u}^d(\mathbf{x}, t + \delta t) - \mathbf{u}^*(\mathbf{x}, t + \delta t)}{\delta t}. \quad (15)$$

#### 2.3.3. Momentum exchange method

Niu et al. [23] proposed a momentum exchange method to compute the IB force. By using the Lagrange interpolation polynomial, the LB distribution functions of all lattice particle directions at the IB points are calculated. Hence, a new set of distribution functions at the IB points could be achieved through the bounce-back rules

$$f_\beta(\mathbf{X}_\beta, t) = f_\alpha(\mathbf{X}_\alpha, t) - 2\omega_\alpha \rho \frac{\mathbf{e}_\alpha \cdot \mathbf{U}_\beta}{c_s^2}, \quad (16)$$

where  $\beta$  denotes the opposite direction of  $\alpha$ ;  $\mathbf{U}_\beta = \mathbf{U} + \mathbf{\Theta} \times (\mathbf{X}_\beta - \mathbf{M})$  is the velocity of the boundary with  $\mathbf{U}$  and  $\mathbf{\Theta}$  representing the translational and angular velocity of the rigid body, respectively;  $\mathbf{M}$  is the mass center of the body;  $\mathbf{X}_\beta$  is its boundary position;  $\omega_\alpha$  are the coefficients in the equilibrium distribution functions. Consequently, the IB force density can be calculated via the momentum exchange

$$\mathbf{F}(\mathbf{X}_\beta, t) = \sum_\beta e_\beta [f_\beta(\mathbf{X}_\beta, t) - f_\alpha(\mathbf{X}_\alpha, t)]. \quad (17)$$

#### 2.3.4. Velocity correction method

For the above three methods, the IB speed cannot be equal to the fluid velocity at the corresponding position due to insufficient interpolation accuracy. This means that non-slip boundary condition cannot be accurately satisfied at solid walls. In order to overcome this drawback, Wu and Shu [26] proposed a velocity correction IB-LB coupling scheme. It is based on the LB equation with external forcing term proposed by Guo et al. [28]. Guo's approach may be expressed as

$$f_\alpha(\mathbf{x} + \mathbf{e}_\alpha \delta t, t + \delta t) - f_\alpha(\mathbf{x}, t) = -\Omega + \delta t F_\alpha, \quad (18)$$

$$F_\alpha = \left(1 - \frac{1}{2\tau}\right) \omega_\alpha \left( \frac{\mathbf{e}_\alpha - \mathbf{u}}{c_s^2} + \frac{\mathbf{e}_\alpha \cdot \mathbf{u}}{c_s^4} \cdot \mathbf{e}_\alpha \right) \cdot \mathbf{f}, \quad (19)$$

$$\rho \mathbf{u} = \sum_\alpha \mathbf{e}_\alpha f_\alpha + \frac{1}{2} \mathbf{f} \delta t, \quad (20)$$

where  $\mathbf{f}$  is the force density at the Eulerian nodes, which is calculated from the Lagrangian IB force at IB points;  $\omega_\alpha$  are weighting factors.

For the velocity correction method, Wu defined the intermediate velocity  $\mathbf{u}^* = \frac{1}{\rho} \sum_\alpha \mathbf{e}_\alpha f_\alpha$  and the velocity correction  $\delta \mathbf{u} = \frac{1}{2\rho} \mathbf{f} \delta t$ . The fluid velocity  $\mathbf{u}$  that corresponds to the IB position may be expressed as

$$\mathbf{u} = \mathbf{u}^* + \delta \mathbf{u}. \quad (21)$$

Thus, the external force is  $\mathbf{f} = 2\rho \delta \mathbf{u} / \delta t$ . The value of  $\delta \mathbf{u}$  can be computed from a system of linear equations derived from the interpolation and spreading of the discrete form of Eq. (21). Although the computing accuracy may be insufficient due to using the Dirac delta function in the interpolation (verified in Section 4.4), it is adequate to ensure that fluid does not penetrate through the solid body. In addition, the coefficient matrix of the equation system is related to the number of IB points  $N$ . For two-dimensional and three-dimensional problems, the matrix size are  $(2N_b)^2$  and  $(3N_b)^2$ , respectively, therefore the memory consumption and computing time will increase significantly as  $N_b$  increases. This imposes limitations on the Lagrangian grid resolution of the IB discretization.

### 3. Iterative force correction IB–LB coupling scheme

In this paper, a new iterative force correction IB–LB coupling scheme is proposed. It is based on the LB equation with external forcing term proposed by Cheng and Li [29]. Cheng’s approach (Eq. (10)) does not need to modify the velocity term, and only need to split the external forcing term into two parts: effects of the present step and the next time step. Substituting Eq. (10) into the LB Eq. (8), we can get the following expression:

$$f_{\alpha}^d(\mathbf{x} + \mathbf{e}_{\alpha}\delta t, t + \delta t) - f_{\alpha}^d(\mathbf{x}, t) = \Omega + \frac{\delta t}{2} [g_{\alpha}^d(\mathbf{x}, t) + g_{\alpha}^d(\mathbf{x} + \mathbf{e}_{\alpha}\delta t, t + \delta t)], \quad (22)$$

where  $\Omega = -M^{-1}\hat{S}[m_{\alpha}(\mathbf{x}, t) - m_{\alpha}^{eq}(\mathbf{x}, t)]$ , and superscript  $d$  denotes the desired reference values which satisfy the non-slip boundary condition.

In Eq. (22), the next time forcing term  $g_{\alpha}^d(\mathbf{x} + \mathbf{e}_{\alpha}\delta t, t + \delta t)$  is unknown. We define an intermediate forcing term  $g_{\alpha}^*(\mathbf{x} + \mathbf{e}_{\alpha}\delta t, t + \delta t)$ , substitute it into Eq. (22), and obtain the expression

$$f_{\alpha}^*(\mathbf{x} + \mathbf{e}_{\alpha}\delta t, t + \delta t) - f_{\alpha}^d(\mathbf{x}, t) = \Omega + \frac{\delta t}{2} [g_{\alpha}^d(\mathbf{x}, t) + g_{\alpha}^*(\mathbf{x} + \mathbf{e}_{\alpha}\delta t, t + \delta t)], \quad (23)$$

where  $f_{\alpha}^*(\mathbf{x} + \mathbf{e}_{\alpha}\delta t, t + \delta t)$  is the intermediate distribution functions at the next time step.

Subtracting Eq. (23) from (22) leads to a new expression

$$f_{\alpha}^d(\mathbf{x} + \mathbf{e}_{\alpha}\delta t, t + \delta t) - f_{\alpha}^*(\mathbf{x} + \mathbf{e}_{\alpha}\delta t, t + \delta t) = \frac{\delta t}{2} (g_{\alpha}^d(\mathbf{x} + \mathbf{e}_{\alpha}\delta t, t + \delta t) - g_{\alpha}^*(\mathbf{x} + \mathbf{e}_{\alpha}\delta t, t + \delta t)). \quad (24)$$

Summing the moments of Eq. (24) [31], we can obtain

$$\begin{aligned} \mathbf{u}^d(\mathbf{x} + \mathbf{e}_{\alpha}\delta t, t + \delta t) - \mathbf{u}^*(\mathbf{x} + \mathbf{e}_{\alpha}\delta t, t + \delta t) &= \frac{\delta t}{2} \left( \sum_{\alpha} \mathbf{e}_{\alpha} g_{\alpha}^d(\mathbf{x} + \mathbf{e}_{\alpha}\delta t, t + \delta t) - \sum_{\alpha} \mathbf{e}_{\alpha} g_{\alpha}^*(\mathbf{x} + \mathbf{e}_{\alpha}\delta t, t + \delta t) \right) \\ &= \frac{\delta t}{2} (\mathbf{f}^d(\mathbf{x} + \mathbf{e}_{\alpha}\delta t, t + \delta t) - \mathbf{f}^*(\mathbf{x} + \mathbf{e}_{\alpha}\delta t, t + \delta t)), \end{aligned} \quad (25)$$

where  $\mathbf{u}^d$  is the desired reference fluid velocity,  $\mathbf{u}^*$  is the intermediate fluid velocity, and  $\mathbf{f}^d$  and  $\mathbf{f}^*$  are the fluid flow external force.

Eq. (25) may be rewritten as the correction form for fluid flow external force:

$$\mathbf{f}^d(\mathbf{x} + \mathbf{e}_{\alpha}\delta t, t + \delta t) = \mathbf{f}^*(\mathbf{x} + \mathbf{e}_{\alpha}\delta t, t + \delta t) + 2 \frac{\mathbf{u}^d(\mathbf{x} + \mathbf{e}_{\alpha}\delta t, t + \delta t) - \mathbf{u}^*(\mathbf{x} + \mathbf{e}_{\alpha}\delta t, t + \delta t)}{\delta t}. \quad (26)$$

In order to satisfy the non-slip condition at the boundary, the IB speed must equal to the fluid velocity at the corresponding position. According to Eqs. (3) and (4), by assuming that Eq. (26) is also valid at the IB points, we can obtain

$$\mathbf{F}^d(\mathbf{X}_l, t) = \mathbf{F}^*(\mathbf{X}_l, t) + 2 \frac{\mathbf{U}^d(\mathbf{X}_l, t) - \mathbf{U}^*(\mathbf{X}_l, t)}{\delta t}. \quad (27)$$

Note that Eq. (27) is the iterative formula for boundary force correction. Here  $\mathbf{U}^d$  is the desired reference boundary speed, and  $\mathbf{U}^*$  is the intermediate boundary speed. When  $\mathbf{U}^*$  is equal to the reference speed  $\mathbf{U}^d$ , Eq. (27) becomes

$$\mathbf{F}^*(\mathbf{X}_l, t) = \mathbf{F}^d(\mathbf{X}_l, t). \quad (28)$$

Considering Eq. (4), we get

$$\mathbf{f}^*(\mathbf{x} + \mathbf{e}_{\alpha}\delta t, t + \delta t) = \mathbf{f}^d(\mathbf{x} + \mathbf{e}_{\alpha}\delta t, t + \delta t). \quad (29)$$

We can regard equation  $|\mathbf{U}^d(\mathbf{X}_l, t) - \mathbf{U}^*(\mathbf{X}_l, t)| = 0$  as the condition which forces the IB force and fluid flow force match their desired values (i.e. Eqs. (28) and (29)).

In the exiting IB–LB coupling schemes, the interaction between fluid and boundary is implemented by the discrete Dirac delta function, which spreads the IB force to the nearby fluid nodes and interpolates IB speed from the local fluid velocity. In this work, the delta function is only used in the force spreading process, and it is replaced by the Lagrange interpolation polynomial in the velocity interpolation process. The interpolation of boundary speed  $U_l(\mathbf{X}_l, t)$  can be expressed as

$$U_l(\mathbf{X}_l, t) = \sum_{ij} \left( \prod_{m=1, m \neq i}^{i_{\max}} \frac{X_l - X_{mj}}{X_{ij} - X_{mj}} \right) \left( \prod_{n=1, n \neq j}^{j_{\max}} \frac{Y_l - Y_{in}}{Y_{ij} - Y_{in}} \right) u_{ij}(\mathbf{x} + \mathbf{e}_{\alpha}\delta t, t + \delta t), \quad (30)$$

where  $i_{\max}$  and  $j_{\max}$  are the maximum numbers of the fluid nodes in the  $x$ - and  $y$ -directions, respectively. Only the nodes within the IB layer (the spreading band of IB force) are involved in calculation, and the width of IB layer is set as  $|\mathbf{x}_{ij} - \mathbf{x}_{pj}| \leq 2$ , in which the subscript  $p$  denotes the running indices  $m$  or  $n$  in Eq. (30).

Fig. 1 is the flow chart for the iterative correction of the IB force, where superscript  $s$  denotes the iteration step with its upper limit  $N$  ( $N \in [10 \sim 20]$ , discussed in Section 4.2). At simulation time step  $n + 1$ , each iteration cycle ( $s = 1, \dots, N$ ) consists of the following steps:

- (1) Correct the boundary force  $\mathbf{F}_{l, n+1}^{(s-1)}$  by using formula (27). Set  $\mathbf{F}_{l, n+1}^{(0)} = 0$  when  $s = 1$ , i.e.  $\mathbf{F}_{l, n+1}^{(1)} = 2 \frac{\mathbf{U}_l^d - \mathbf{U}_l^{(0)}}{\delta t}$ .
- (2) Spread the corrected IB force  $\mathbf{F}_{l, n+1}^{(s)}$  to the fluid external force  $\mathbf{f}_{ij, n+1}^{(s)}$  by using formula (4).
- (3) Calculate the forcing distribution function  $g_{\alpha, n+1}^{(s)}$  from the fluid external force  $\mathbf{f}_{ij, n+1}^{(s)}$  by using formula (11). Set  $\mathbf{u}_{ij, n+1}^{(0)} = \mathbf{u}_{ij, n}^{(N)}$  when  $s = 1$ .  $g_{\alpha, n}^{(s)}$  has already been obtained at the time step  $n$ . At  $n = 0$  time step, we may initialize  $g_{\alpha, 0}^{(s)} = 0$ .
- (4) Calculate the fluid flow velocity  $\mathbf{u}_{ij, n+1}^{(s)}$  within the IB layer (the area surrounded by the black dash lines in Fig. 1) by formula (9).
- (5) Interpolate the IB speed  $\mathbf{U}_l^{(s)}$  from the local fluid velocity  $\mathbf{u}_{ij, n+1}^{(s)}$  by using formula (30).
- (6) Compare the difference of IB speed between the simulated value  $\mathbf{U}_l^{(s)}$  and the reference value  $\mathbf{U}_l^{(d)}$ . If  $\|\mathbf{U}_l^{(s)} - \mathbf{U}_l^{(d)}\| < \varepsilon$ , or  $s$  reaches the given maximum iteration time  $N$ , one may identify the convergence and just let  $\mathbf{U}_l^{(s)} = \mathbf{U}_l^{(d)}$ .
- (7) If the convergence condition  $\|\mathbf{U}_l^{(s)} - \mathbf{U}_l^{(d)}\| < \varepsilon$  is not satisfied and  $s < N$ , one should repeat the step (1) to step (7) until the convergence is reached.

### 4. Numerical verification

#### 4.1. Overall spatial convergence order

The MRT-LB model was adopted in the present work for modeling the flow field. It is evident that the MRT-LB model has a second-order spatial accuracy. When the LB model is combined with the IB model, the discretized Dirac delta function, with the first-order accuracy, spreads the boundary force to the nearby fluid nodes. Although the spreading or interpolation is only applied in the

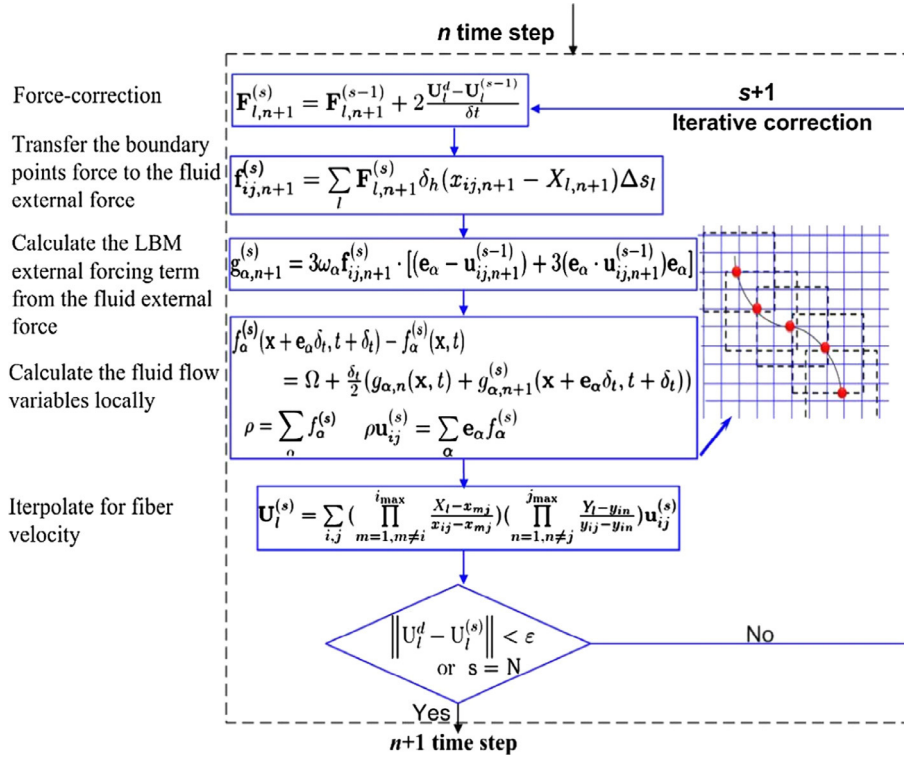


Fig. 1. Flow chart of iterative correction procedure for  $f_{ij,n+1}^{(s)}$  at evolution time step  $n$ .

region nearby the boundary, it may affect the global accuracy of solution in the whole domain.

The double-sided shearing flow, which has been discussed in Ref. [27], was selected as a typical case for accessing the overall accuracy. A straight fiber moving longitudinally at a constant speed  $U = 0.1$  is placed in the middle of a square flow domain, and conducts a triangular flow velocity distribution in the whole domain. The computational domain was discretized to  $L \times L$  nodes ( $L = 40, 80, 160, 320 \Delta x$ ), and the spacing of the adjacent IB points  $\Delta s = 0.5 \Delta x$ . The two side boundaries are set as walls while the top and bottom flow boundaries are set to be periodic. The overall error of velocities was evaluated by the following  $L_{\text{error}}$

$$L_{\text{error}} = \frac{\sqrt{\sum_{N_{\text{node}}} (u_{ij}^c - u_{ij}^a)^2}}{N_{\text{node}}}, \quad (31)$$

where  $u_{ij}^c$  and  $u_{ij}^a$  represent the simulated velocity and exact solution at the steady state ( $|L_{\text{error}}^{n+1} - L_{\text{error}}^n| < 10^{-7}$ ), respectively.  $N_{\text{node}}$  is the total number of the fluid nodes in the whole domain. The problem is simulated by the new method with the maximum number of iterations  $N = 10$  (discussed in Section 4.2). The results are plotted in Fig. 2. When the parameter  $L \leq 80$  and  $80 < L \leq 160$ , the slopes of the line are about 0.86 and 0.92, respectively. However, the overall accuracy will be first-order if the parameter  $L > 160$ .

#### 4.2. Iteration convergence rate and accuracy for viscous flow

It is necessary to find an efficient number of iterations  $N$  for correcting the IB force. The flow around a stationary circular cylinder is simulated to estimate the iteration time and to verify the effectiveness of the present method. This problem has been extensively studied and there are many experimental and numerical results available. For example, the problem has been used to verify whether the non-slip boundary condition is satisfied by the IB-LB coupling schemes in Refs. [26,32].

The Reynolds number in this flow may be defined as

$$\text{Re} = \frac{u_{\text{inlet}} D}{\nu}. \quad (32)$$

Inlet velocity  $u_{\text{inlet}} = 0.1$ , cylinder diameter  $D = 40$ , fluid mesh  $40D \times 50D$ , and boundary points  $N_b = 250$  were chosen. As Reynolds number increases to a certain value, the vortices shedding will occur with frequency  $f_q$ , which is corresponding to Strouhal number:

$$\text{St} = \frac{f_q D}{u_{\text{inlet}}}. \quad (33)$$

For quantitative estimation of iteration effect, an averaged simulation error  $E_1$  at the IB points is defined as

$$E_1 = \frac{\sqrt{\sum_{l=1}^{N_b} (\bar{U}_{l,r}^c - \bar{U}_{l,r}^d)^2 + (\bar{U}_{l,\theta}^c - \bar{U}_{l,\theta}^d)^2}}{N_b}, \quad (34)$$

where  $\bar{U}_r = U_r / |u_{\text{inlet}}|$  and  $\bar{U}_\theta = U_\theta / |u_{\text{inlet}}|$  are the normalized radial and tangential velocity at the cylinder wall, respectively. The superscript  $c$  and  $d$  denote the numerical values and the desired reference values. The angle  $\theta$  was measured counter-clockwise from the back stagnation point of the cylinder.

The steady flow at  $\text{Re} = 20$  is simulated first. Choosing different iteration times for force correction in every time step, i.e.  $N = 0, 5, 10, 20$ , and  $50$ . We obtain the steady state of this flow through imposing the stopping condition  $|E_{1,n+1} - E_{1,n}| < 10^{-8}$  of the IB-LB simulations. Fig. 3 shows the history of average error  $E_1$  decreases at different iteration times  $N$ . That is to say that the accuracy at boundary walls can be improved by increasing the number of iterations of force correction. According to many different test cases, there is an experience should be shared: for a steady flow, the error is negligible when the number of iterations is greater than 10; however, for an unsteady flow case,

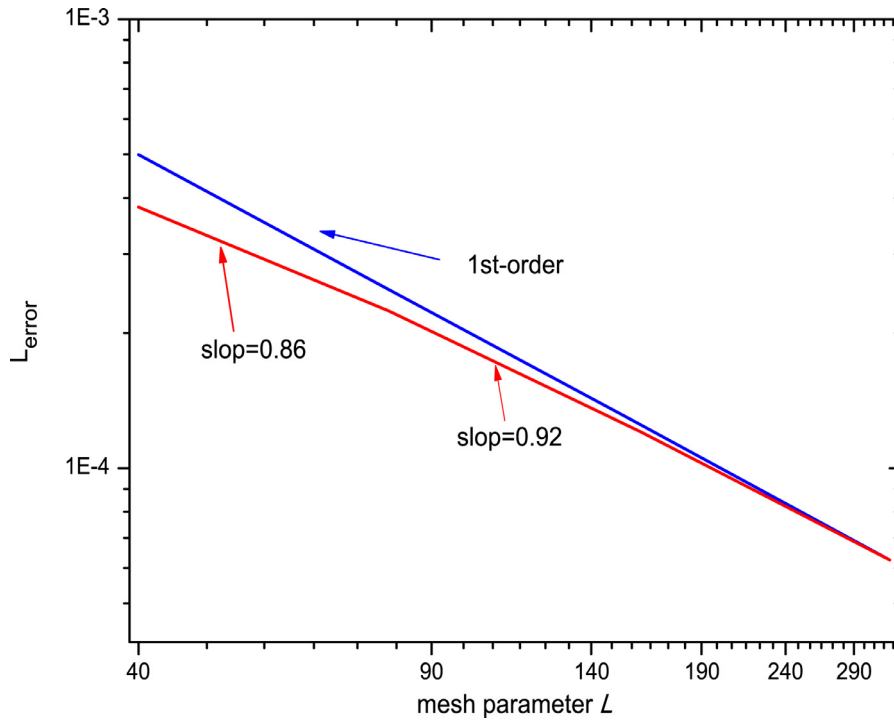


Fig. 2. Spatial convergence order of the force correction IB–LB coupling scheme.

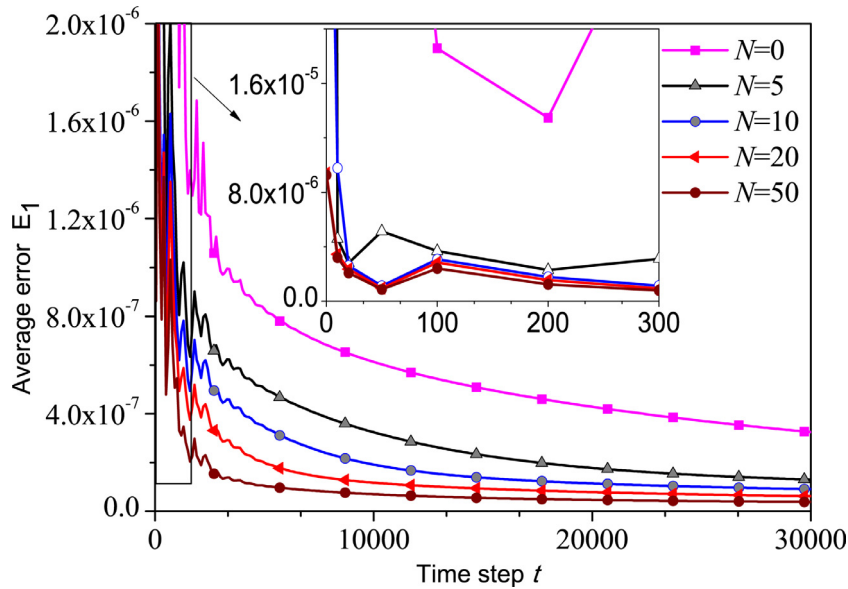


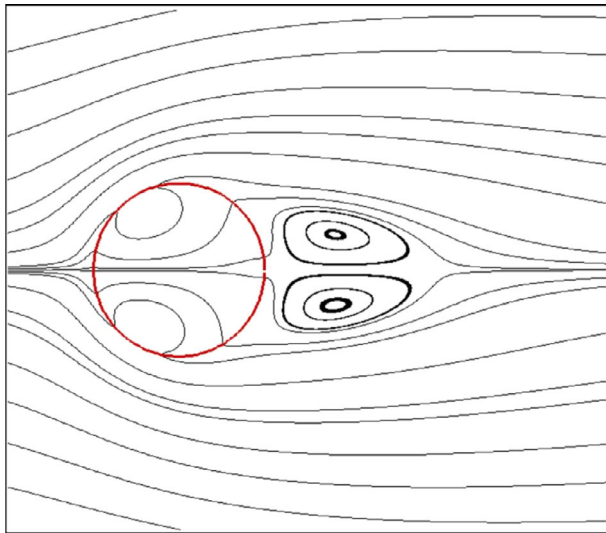
Fig. 3. The history of average error at different iteration times for  $Re = 20$  flow around a cylinder.

$N = 20$  is a better choice. It should be noted that all cases in this paper follow the experience.

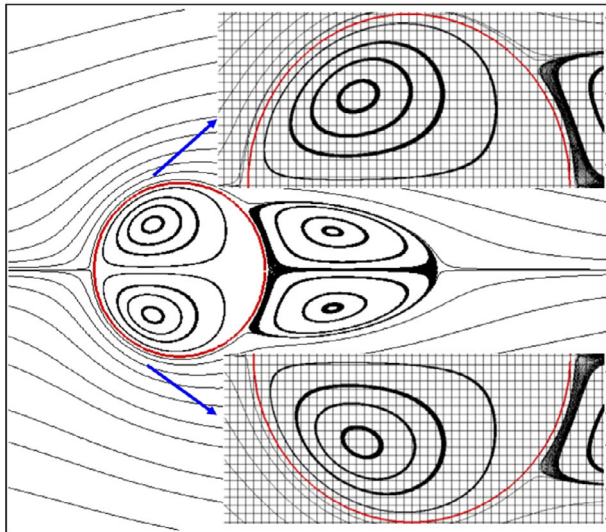
Fig. 4 compares the streamlines by the existing and present methods. Clearly in Fig. 4(b), the streamlines obtained by the present method show no penetration into the cylinder wall. In fact, the streamlines inside the cylinder are totally enclosed by the cylinder wall, and the streamlines outside the cylinder (including the trailing vortex) cling to the cylinder wall (the spaces between the streamlines and the cylinder wall are smaller than  $\sqrt{2}\Delta x$ , which reaches the resolution limit). This means that there is no mass exchange between

the fluid inside and outside the cylinder. In contrast, the streamlines in simulations by the existing methods (except for the velocity correction method) cross the cylinder wall, and the trailing vortex stays away from the cylinder wall. Fig. 4(a) is the results by the direct forcing IB–LB scheme, and other existing IB–LB schemes give similar results. This is because the non-slip boundary condition is accurately enforced by the present method but not by the existing IB–LB schemes.

To further investigate the differences between the present method and the existing methods, the normalized radial velocity



(a) Normalized radial velocity  $\bar{U}_r$



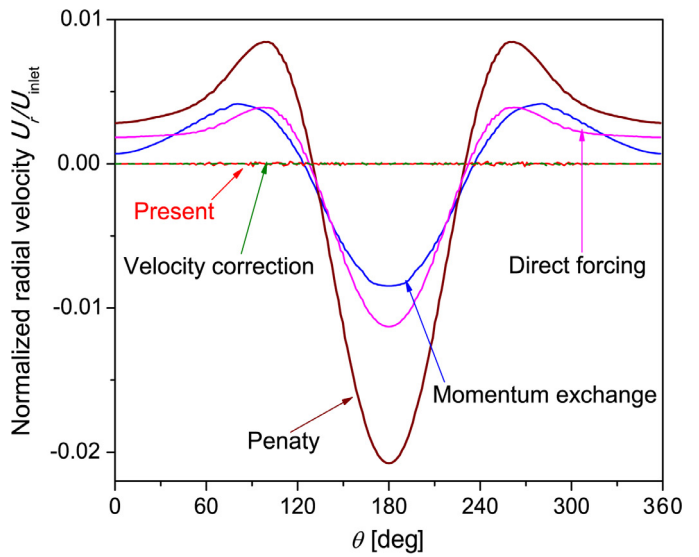
(b) Normalized tangential velocity  $\bar{U}_\theta$

**Fig. 4.** Comparison of streamlines for  $Re = 20$  flow around a cylinder. (a) Streamlines penetrate the cylinder wall by direct forcing IB–LB scheme; (b) No streamlines penetrate the cylinder wall by present IB–LB scheme.

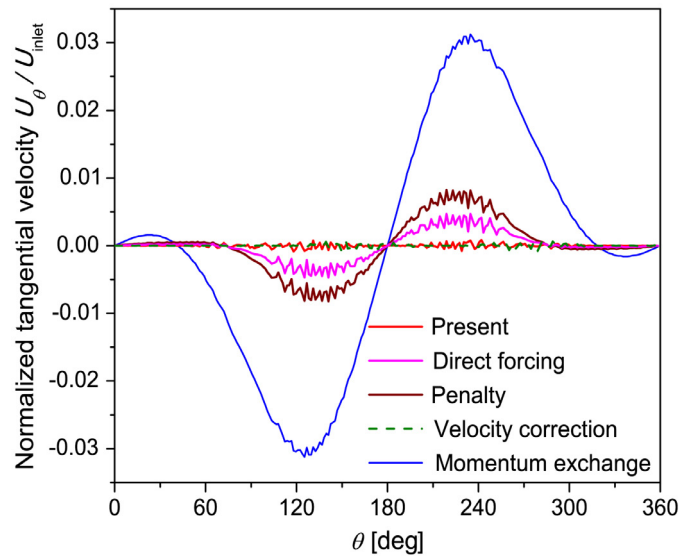
$\bar{U}_r$  and normalized tangential velocity  $\bar{U}_\theta$  at the cylinder wall are shown in Fig. 5. The  $\bar{U}_r$  and  $\bar{U}_\theta$  simulated by the present method are much smaller than those by the direct forcing, penalty and momentum exchange methods, with the average error  $E_1 = 0.00012$  for the former,  $E_1 \in [0.0043 \sim 0.026]$  for the latter three. The results by the velocity correction method are also accurate, with  $E_1 = 0.00015$ . Fig. 6 shows the amplified curves of  $\bar{U}_r$  and  $\bar{U}_\theta$  by the present method. Fluctuations of velocities, especially  $\bar{U}_\theta$ , are obvious within  $\theta \in [50, 150]$  and  $\theta \in [200, 300]$ . However, the maximum fluctuation amplitudes  $|\bar{U}_r|_{\max}$  and  $|\bar{U}_\theta|_{\max}$  are only 0.0002 and 0.0008, respectively, in the similar level if they are compared with 0.0003 and 0.0004 by the interpolated bounce-back scheme [32]. The obvious fluctuation location corresponds to the strong shearing flow regions, while those near the stagnation points are relative weak. Meanwhile, fluctuation in  $\bar{U}_\theta$  is more intense than that of  $\bar{U}_r$ . In addition, an unsteady flow with  $Re = 200$  is simulated, and the average error  $E_1$  at cylinder wall averaged over a shedding cycle by different IB–LB meth-

ods are presented here. The present and velocity correction method yield the smallest errors  $E_1 = 0.00051$ , and the other three methods obtain a larger error  $E_1 \in [0.014 \sim 0.096]$ . Note that the flow velocity near the solid wall is one of the main factors which affect the accuracy of the present method, because an interpolation is used in calculating IB velocity from the local fluid velocity.

The Strouhal numbers of circular cylinder flows at  $Re = 80, 100$  and  $200$  are also simulated. Table 1 Comparison of the predicted Strouhal number with previous related data for different Reynolds numbers. The predicted Strouhal numbers agree very well with the previous experimental and numerical data [33–37], and are almost the same as those in the experiment of Williamson [34]. These demonstrate the reliability of the proposed IB–LB coupling scheme.



(a) Normalized radial velocity  $\bar{U}_r$



(b) Normalized tangential velocity  $\bar{U}_\theta$

**Fig. 5.** Comparison of the normalized velocities on cylinder surface at  $Re = 20$ . (a) Normalized radial velocity  $\bar{U}_r$ ; (b) Normalized tangential velocity  $\bar{U}_\theta$ .

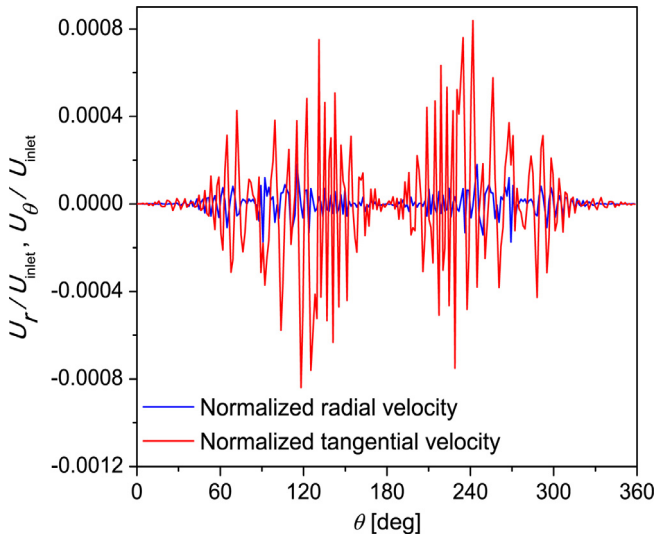


Fig. 6. Normalized velocity on cylinder surface simulated by the present method at  $Re = 20$ .

Table 1  
Comparison of the predicted Strouhal number with previous related data for different Reynolds numbers.

Re	Present	Ref. [34](Exp.)	Ref. [35]	Ref. [36]	Ref. [37]	Ref. [33]
80	0.149	0.150	0.150	–	0.153	0.153
100	0.164	0.166	0.160	0.165	0.168	0.166
200	0.196	0.197	–	0.190	–	0.196

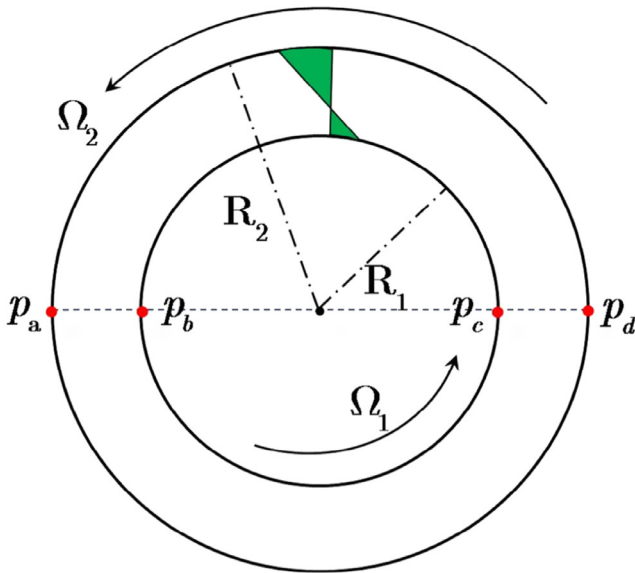


Fig. 7. Schematic diagrams of the circular Couette flow between two inversely rotating cylinders.

4.3. Accuracy for strong shearing flow

The non-physical wall slip may be observed when simulating strong shearing flows by the existing method [38,27]. We try to check whether the phenomenon could be eliminated by the present method through simulating the circular Couette flow between two inversely rotating cylinders. As shown in Fig. 7, a special feature of this case is that the two cylinders (represented by two circular fibers) rotate in opposite directions. Consequently, severe shearing along the circular boundaries occurs, which leads to a velocity inversion be-

tween the two cylinders. The analytical solution of the laminar circular Couette flow may be found in [27].

When let the radii  $R_1 = 40$  and  $R_2 = 60$ , and rotational angular speeds  $\Theta_1 = -0.1/40$  and  $\Theta_2 = 0.15/60$  for the inner and outer cylinders, respectively, the corresponding peripheral speeds will be  $U_{\theta,inner} = -0.1$  and  $U_{\theta,outer} = 0.15$ . These parameters are in the lattice unit. The two cylinders, represented by fibers with  $N_b = 550$  and  $N_b = 800$  IB points, respectively, were placed at the center of a computational domain of  $N_x \times N_y = 400 \times 400$  nodes. The Dirichlet boundary conditions of pressure  $p = 1/3$  for the four sides, and the fluid viscosity  $\nu = 1.0$  were applied.

Fig. 8 depicts the normalized radial velocity  $\bar{U}_r = U_r/|U_{\theta,inner}|$  and normalized tangential velocity  $\bar{U}_\theta = U_\theta/|U_{\theta,inner}|$  at the inner cylinder wall.  $\bar{U}_r$  and  $\bar{U}_\theta$  fluctuate around the desired values (0.0,1.0), and the maximum error are  $|\bar{U}_r|_{max} = 1.5 \times 10^{-4}$  and  $|\bar{U}_\theta|_{max} = 5.7 \times 10^{-4}$ , respectively. These fluctuations can be obviously observed near the four diagonal regions where the IB boundary is not perpendicular or parallel to the fluid mesh lines. However, the error magnitude is only of the order of  $10^{-7}$  in other regions. This verifies that the IB orientation with the fluid mesh has important effect on the accuracy of the IB-LB schemes.

Fig. 9 shows  $\bar{U}_r$  and  $\bar{U}_\theta$  distributions along the inner cylinder wall simulated by the different IB-LB schemes. The normalized average error obtained by the present method ( $E_1 = 0.00031$ ) has the same order of magnitude as the one simulated by the velocity correction method ( $E_1 = 0.00039$ ), which are both far smaller than those of other three methods ( $E_1 \in [0.0037,0.058]$ ).

The velocity profiles of  $y$ -component along the center horizontal line  $y = 200$  are plotted in Fig. 10. The results by the present method, especially inside the inner cylinder (between  $p_b$  and  $p_c$ ) are far closer to the theoretical solutions than those by other methods. In order to compare the differences between the numerical and theoretical solutions intuitively, the relative error  $E_r$  is defined as

$$E_r = \frac{|u_\theta^a - u_\theta^c|}{|u_\theta(40)|}, \tag{35}$$

in which, the superscript  $a$  and  $c$  denote the theoretical and the numerical values, respectively. As depicted in Fig. 11, at IB points  $p_a$ ,  $p_b$ ,  $p_c$ , and  $p_d$ , the velocity correction method results in the largest  $E_r = 0.07$ , and the present method yields the smallest  $E_r = 1.1 \times 10^{-6}$ . Between points  $p_a$  and  $p_b$  (or  $p_c$  and  $p_d$ ),  $E_r$  values are relative large, with the maximum  $E_r \in [0.17,0.21]$  for the four conventional methods and the maximum  $E_r = 0.13$  for the present method. Inside the inner cylinder (between points  $p_b$  and  $p_c$ ), the maximum  $E_r \in [0.05,0.12]$  for the four methods and the maximum  $E_r = 0.04$  for the present method. Therefore, the present method has better accuracy in treating the non-slip boundary of strong shear flow compared to other IB-LB coupling schemes.

4.4. Accuracy for high viscous flow

Boundary slip and incorrect velocity profiles in shearing flow have been discussed in Refs. [38,27] and shown in the last case. As the kinematic viscosity increases, the non-physical slip and profile deviation become more severe. The viscosity sensitivity of the present method was verified by the double-sided shearing flow.

As mentioned at Section 4.1, the computational domain was discretized by  $N_x \times N_y = 100 \times 100$  nodes, and the fiber was represented by  $N_b = 250$  uniformly distributed IB points. The two side

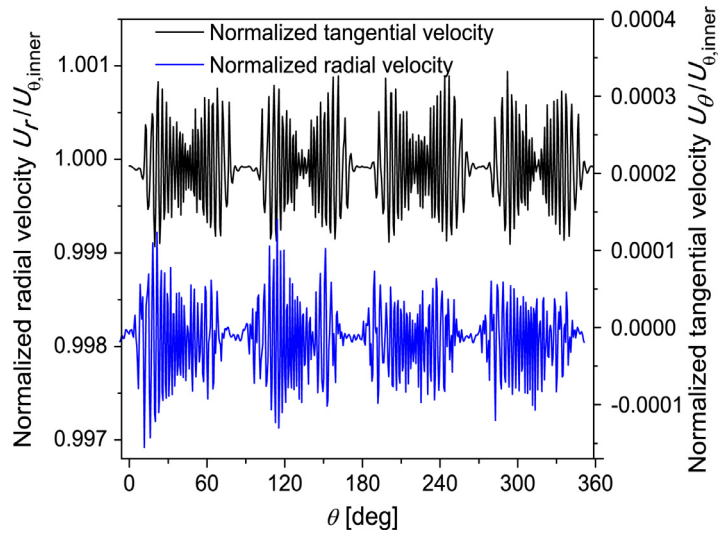
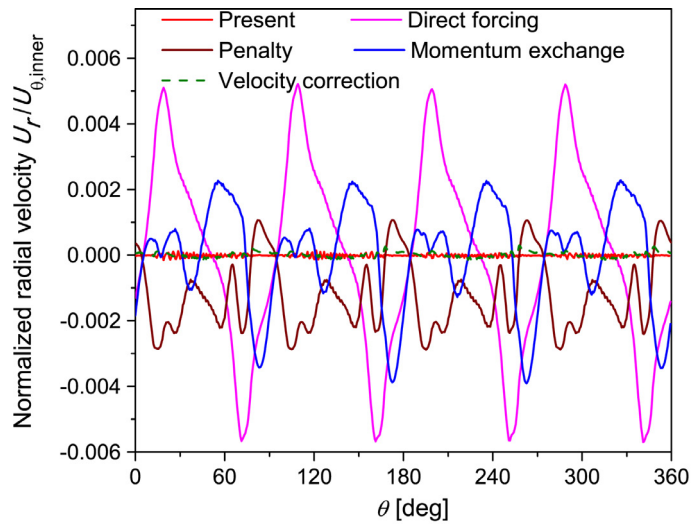
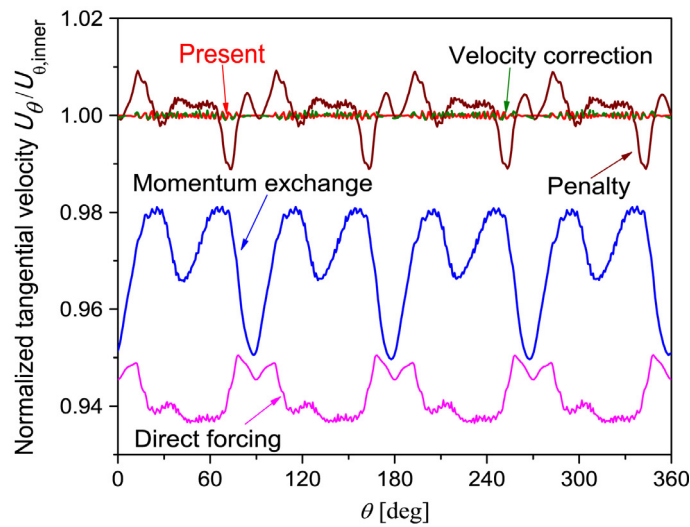


Fig. 8. Normalized velocity at inner cylinder wall simulated by the present method.



(a) Normalized radial velocity  $\bar{U}_r$



(b) Normalized tangential velocity  $\bar{U}_{\theta}$

Fig. 9. Comparison of the normalized velocity at inner cylinder wall with  $\nu = 1.0$ . (a) Normalized radial velocity  $\bar{U}_r$  (b) Normalized tangential velocity  $\bar{U}_{\theta}$ .

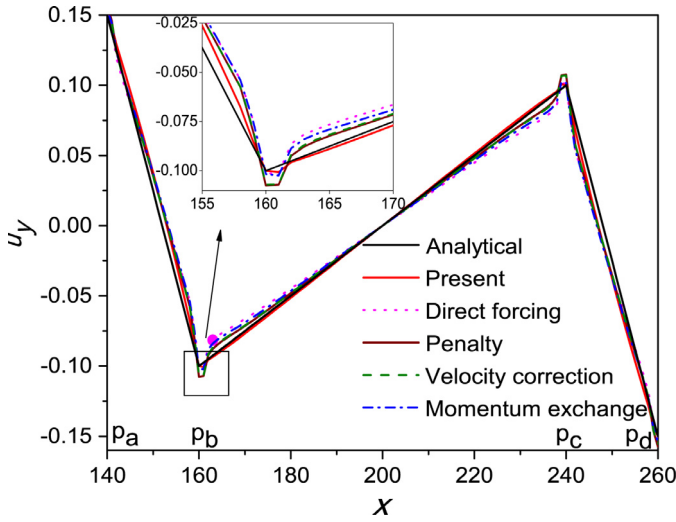


Fig. 10. Comparison of the y-component of velocity along the center horizontal line  $y = 200$ .

boundaries are set as walls while the top and bottom flow boundaries are set to be periodic.

Theoretically, the flow nodes coincide with the moving fiber (denoted as “F nodes”) should have the same velocity as the IB speed, namely  $u(x,y) = (0,0.1)$ , and the velocity profiles should be straight lines and independent of viscosity of the fluid. We define the average error  $E_2$  as

$$E_2 = \frac{\sum_{i=0}^{NX} |u_{i,y}^a - u_{i,y}^c|}{N_b}, \quad (36)$$

where the superscript  $a$  and  $c$  denote the theoretical and the numerical value, respectively.

The test case is simulated by the existing and present methods considering kinematic viscosity  $\nu = 0.5, 1.0, 2.0$  and  $5.0$ . The flow velocity components  $u_y(x)$  along the center horizontal line  $y = 50$  are depicted in Fig. 12. Due to the insufficient interpolation accuracy of the Dirac delta function, all the velocities at “F nodes” simulated by the existing methods, including the velocity correction method are not equal to  $u^d(x,y) = (0,0.1)$ . Particularly when  $\nu = 2.0$  and  $5.0$ , significant non-physical profile deviations can be observed. The velocity slips and profile deviations cause the simulation results untrust-

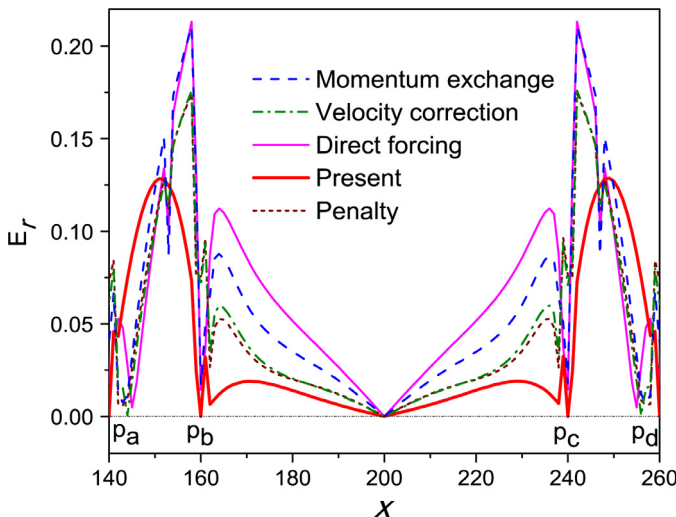


Fig. 11. Comparison of the relative error along the center horizontal line  $y = 200$ .

worthy. The present method will not introduce similar velocity slip at “F nodes” unless the Dirac delta function is used in interpolating IB speed (the line of present (delta) in Fig. 13). Note that only the present method can ensure the velocity at “F nodes” is equal to the theoretical value.

According to Ref. [38], the relaxation parameter  $\tau$  could not be greater than 2 (i.e.  $\nu \leq 0.5$ ) by the existing IB–LB coupling schemes. Fig. 14 illustrates that the average errors simulated by all the five methods with different viscosities (horizontal axis is logarithmic for  $\log_2$ , and the vertical axis is linear). When  $\nu$  is less than 0.5, the average error is in the range of  $[2.24 \times 10^{-4} - 7.7 \times 10^{-4}]$  regardless of which IB–LB coupling schemes are adopted. However, when the viscosity is greater than 0.5, the error obtained by the penalty method increases rapidly and a severe deviation from the theoretical solution is observed. While the errors by the momentum exchange and direct forcing methods have the similar order of magnitude, they are obviously smaller than the one obtained by the penalty method. The error by the present method or velocity correction method is the smallest among all methods.

### 5. Simulation of two-dimensional mechanical heart valve flow

To demonstrate the ability of the proposed method, a typical 2D mechanical heart valve flow [39] is simulated and the numerical results are compared with both experimental data and those simulated by commercial software Fluent and Flow 3D.

#### 5.1. Geometry and physical parameters

The 2D geometry (Fig. 15) consists of an inflow tract (inlet = left ventricle), a sinus of aortic valve, an outflow tract (outlet = aorta), and a rigid valve leaflet. The dimensions of the geometry are  $l_1 = 4$  cm,  $l_2 = 4$  cm,  $r_1 = 2$  cm,  $r_2 = 0.75$  cm,  $h = 2$  cm and  $\theta_{\text{initial}} = 0.384$  rad =  $22^\circ$ . The blood density  $\rho_{\text{blood}} = 1090$  kg/m<sup>3</sup>, and the dynamic viscosity  $\mu = 4$  m Pa s =  $4 \times 10^{-3}$  kg/(ms). As the inlet boundary condition (Fig. 16), a pulsatile velocity in  $x$ -direction was given by a function of time [39,40]:

$$\text{For } 0 < t < t_0 \text{ and } t_0 + 0.37T_p < t < T_p,$$

$$u_{\text{inlet}} = u_{\text{mean}} + 0.5u_{\text{ampl}} \sin \left\{ \frac{2\pi(t - t_0)/T_p + 0.26}{1.26} \right\}. \quad (37)$$

$$\text{For } t_0 < t < t_0 + 0.37T_p,$$

$$u_{\text{inlet}} = u_{\text{mean}} + u_{\text{ampl}} \sin \left[ \frac{2\pi(t - t_0)/T_p}{0.74} \right]. \quad (38)$$

The parameters in the above two formulas are the initial time  $t_0 = 0.4$  s, the period  $T_p = 2.45$  s, the mean velocity  $u_{\text{mean}} = 0.04$  m/s, and the velocity amplitude  $u_{\text{ampl}} = 0.11$  m/s. Velocity component  $v$  in the  $y$ -direction at the inlet is set as  $v_{y,\text{inlet}} = 0$  m/s. The outlet is set as an outflow boundary condition (the unknown distributions functions are replaced by those located at the neighbor nodes). Other boundaries are set as walls.

The valve leaflet is simulated by the present method, and the torque per unit length is

$$T = I \cdot \theta, \quad (39)$$

where  $\theta$  is the opening angle of the leaflet which is indicated in Fig. 15.  $I$  is the moment of inertia per unit length which can be calculated as

$$I = \frac{1}{3} ml^2, \quad (40)$$

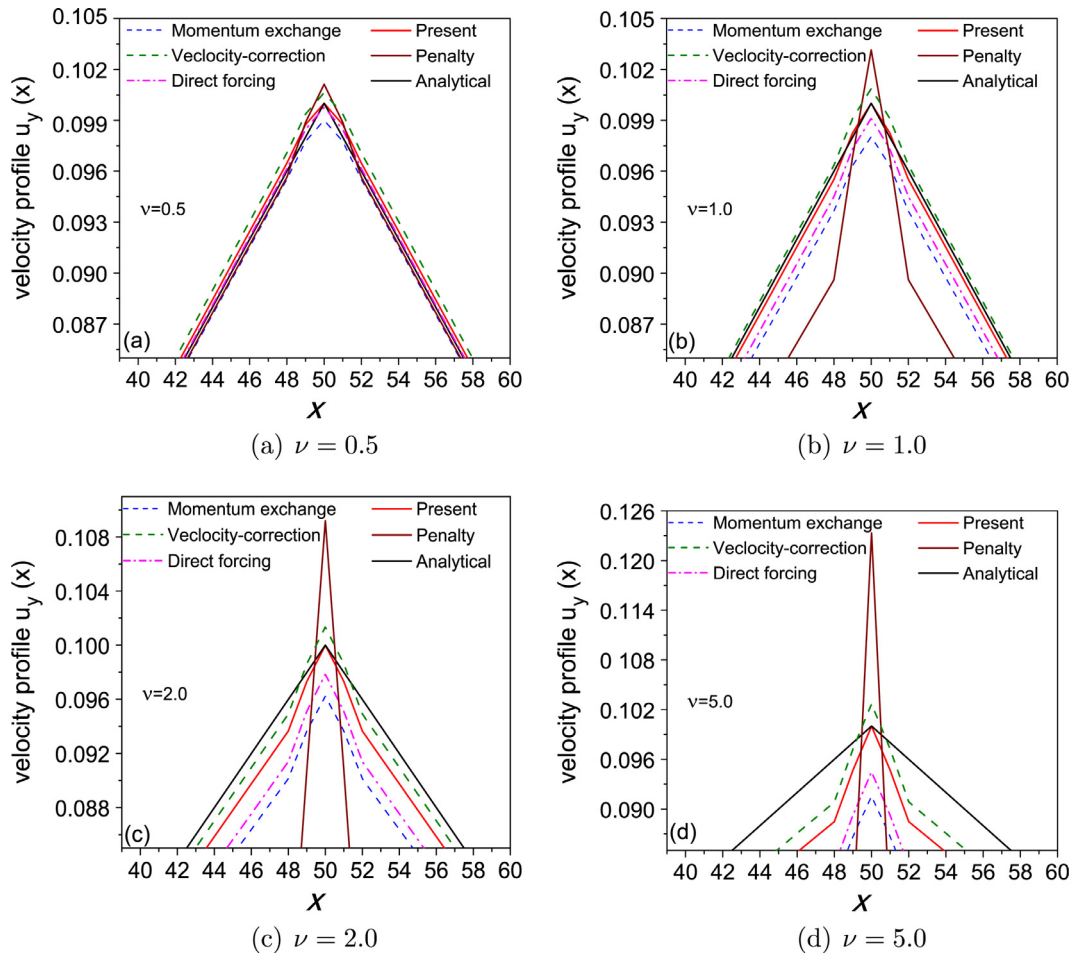


Fig. 12. Velocity profiles along the center horizontal line  $y = 50$  by different methods for different viscosities (a)  $\nu = 0.5$ ; (b)  $\nu = 1.0$ ; (c)  $\nu = 2.0$ ; (d)  $\nu = 5.0$ .

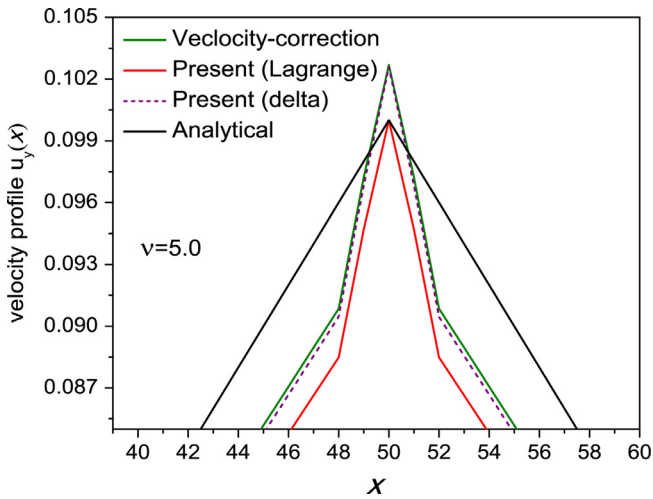


Fig. 13. Comparison of interpolation effect between Dirac delta function and Lagrange interpolation polynomial.

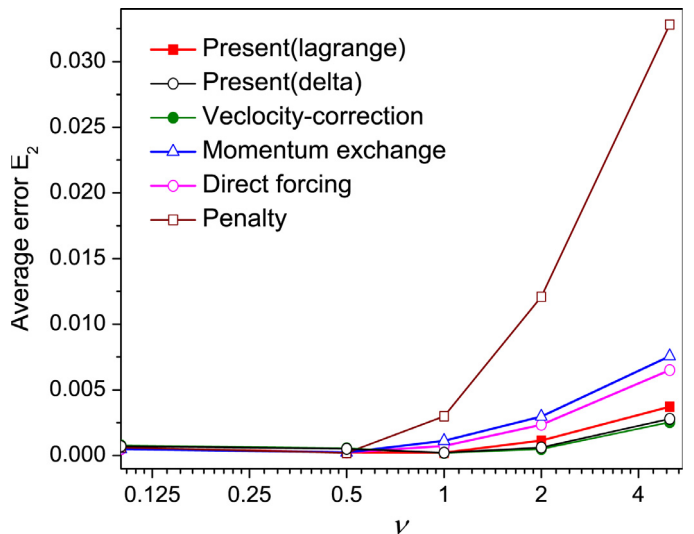


Fig. 14. Average velocity error against viscosity for different methods.

where  $m = \rho_{\text{leaflet}} \cdot l \cdot t$  is the mass of the leaflet per unit length,  $\rho_{\text{leaflet}} = 1100 \text{ kg/m}^3$  is the density of the leaflet,  $t = 1 \text{ mm}$  is the thickness of the leaflet, and  $l = 22 \text{ mm}$  is the length of the leaflet. Thus, the moment of inertia is  $I = 3.9 \times 10^{-6} \text{ kg m}^2$ .

### 5.2. Dependence on cycles and mesh resolution

The flow velocity of the first cycle was initialized with zero in the whole fluid domain, and the next cycles were initialized with the results of the last cycle at  $t = 2.45 \text{ s}$ . Therefore, the

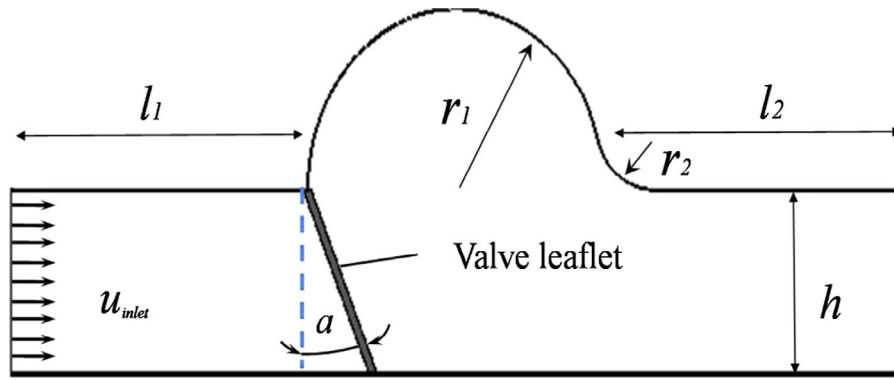


Fig. 15. Geometry of the two-dimensional aortic valve model.

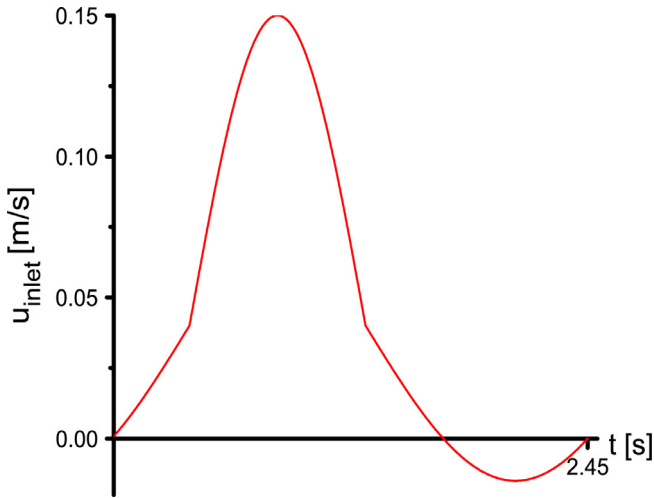


Fig. 16. Velocity boundary condition at the inlet as a function of time  $t$ .

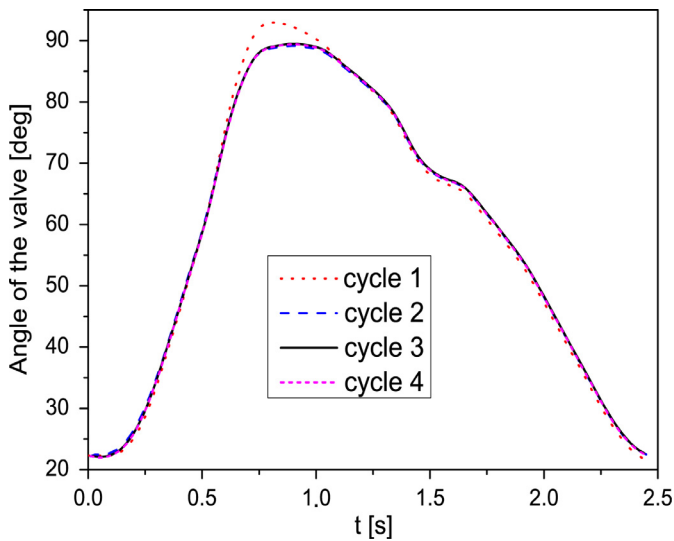


Fig. 17. Evolution of the opening angle of valve for the first four cycles.

cycle-dependence of results should be analyzed. Fig. 17 is the evolution of opening angle of valve for the first four cycles. The curve of the first cycle is obvious different from the late cycles, and the curve of the third cycle overlaps with that of the fourth cycle.

In addition, sensitivity of our results to the Eulerian grid resolution is also investigated by considering three test simulations at different resolutions  $\Delta x = 2.0 \times 10^{-4}$ ,  $1.67 \times 10^{-4}$  and  $1.25 \times 10^{-4}$  (Fig. 18). No significant differences are observed between the test cases as long as the resolution is finer than  $\Delta x = 1.67 \times 10^{-4}$ . Thus, the results in the third cycle, simulated by resolution  $\Delta x = 1.67 \times 10^{-4}$ , are analyzed in the subsequent sections.

### 5.3. Numerical results and discussion

Fig. 19 demonstrates the simulated velocity vectors at five different times during one cycle, which are compared to the corresponding experimental PIV pictures. At the beginning (Fig. 19(a)  $t = 0$  s), two vortices are formed: A large vortex located at the sinus cavity and a smaller secondary vortex near the bottom wall downstream of the leaflet can be found. During the first acceleration stage of the aortic flow, the valve leaflet is pushed towards the aortic sinus, and the vortices become smaller and the secondary vortex is even disappeared (Fig. 19(b)  $t = 0.37$  s). At  $t = 0.88$  s, the inlet pulsatile velocity reaches its maximum value, the opening angle of the leaflet nearly reaches the full opening (Fig. 20), and the large vortex is reduced to a small vortex in the

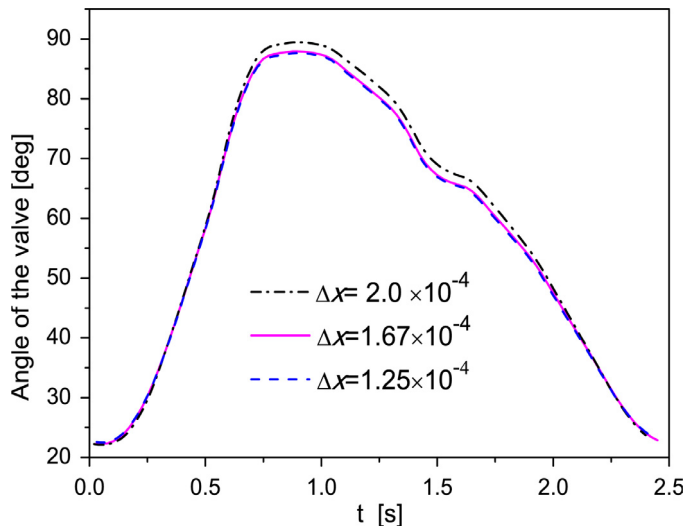


Fig. 18. Comparison of evolution of the opening angle of the valve for different mesh densities.

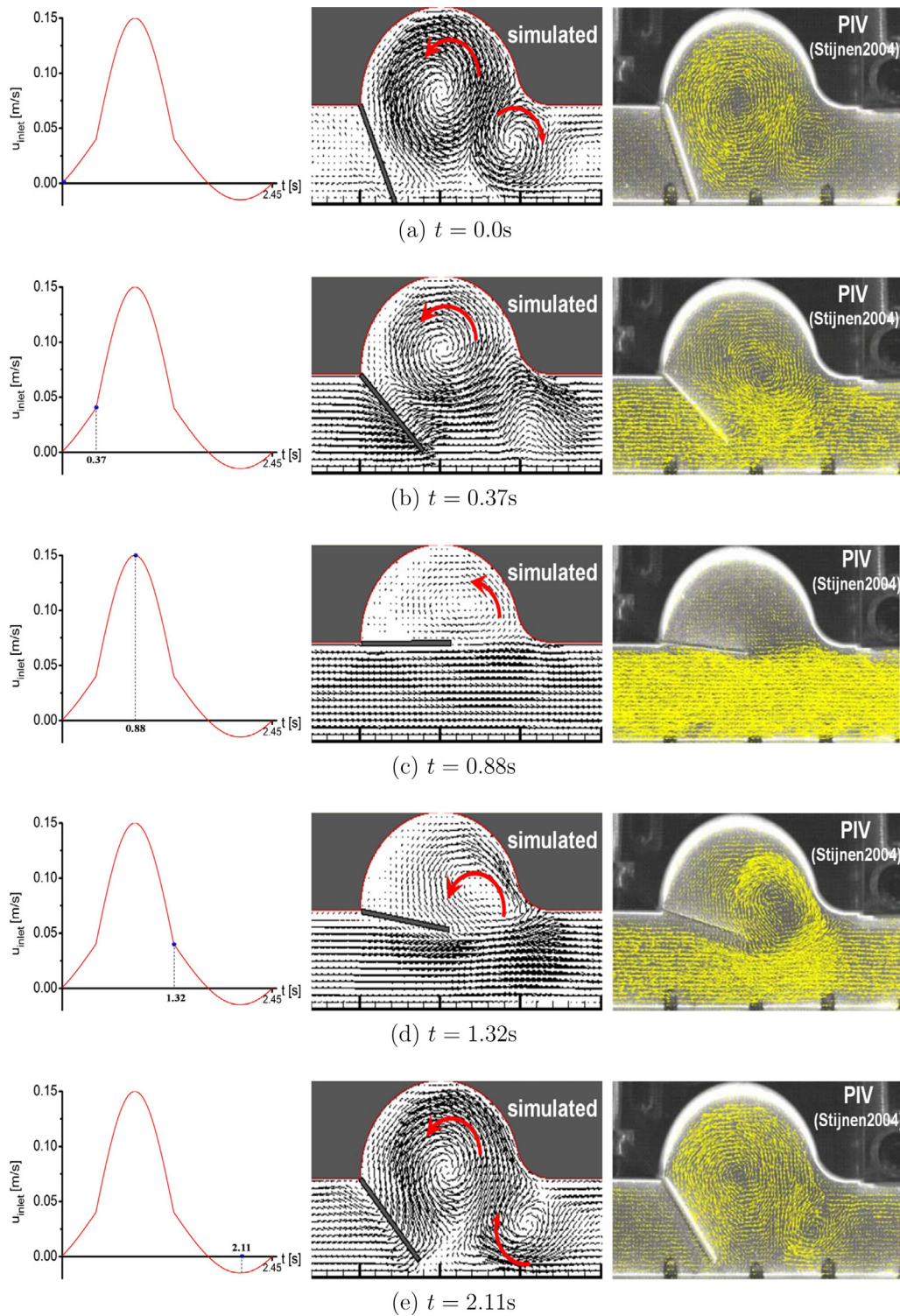


Fig. 19. Velocity vectors for: (a)  $t = 0.0\text{ s}$ ; (b)  $t = 0.37\text{ s}$ ; (c)  $t = 0.88\text{ s}$ ; (d)  $t = 1.32\text{ s}$ ; (e)  $t = 2.11\text{ s}$ .

sinus cavity (Fig. 19(c)). At  $t = 1.32\text{ s}$ , the vortex is almost filling the whole sinus cavity (Fig. 19(d)). Thus, during the closure of the valve, the vortex in the sinus grows. During the further closure of the valve, a second small vortex rotating clockwise has developed at the downstream side of the large vortex.

Comparisons of valve leaflet opening angles are shown Fig. 20. The results simulated by the present method are closer to the experimen-

tal data than those by commercial software Fluent [40,41] and Flow-3D, in terms of the maximum opening angle and its timing, although the numerical leaflet angles are higher than the experimental values. To be specific, the simulated results shows a maximum opening angle  $\theta_{\max} = 87.8^\circ$  at  $t = 0.91\text{ s}$ , while the experimental maximum opening angle is lower, i.e.  $\theta_{\max} = 85.5^\circ$  at  $t = 0.95\text{ s}$ .

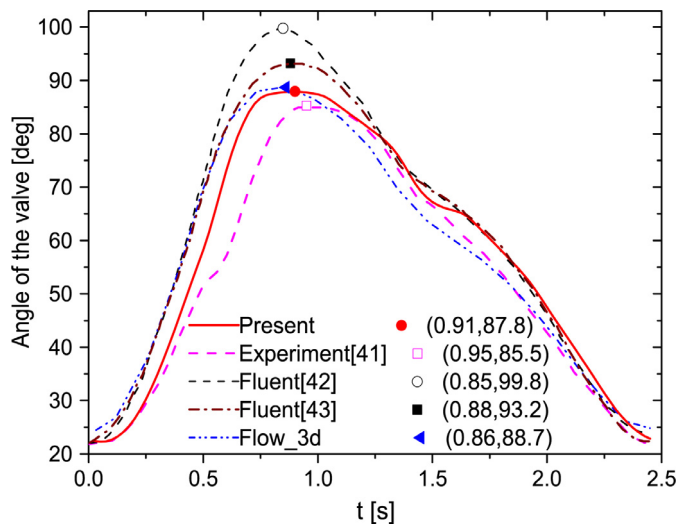


Fig. 20. Comparison of the simulated results with the experimental data.

## 6. Conclusion

To improve simulation accuracy and efficiency at wall boundaries, a new iterative force correction IB–LB coupling scheme is proposed. It is based on the LB equation with the external forcing term proposed by Cheng and Li [29]. The unknown IB force and force on the fluid at the next time step is corrected iteratively, based on the known IB speed and flow velocity, together with the relations between the speed and the force. Although an implicit method, the computer memory and computational cost will not significantly increase because it is only related to the influence range of boundary force but not related to the number of IB points. Four typical test cases are simulated to verify and validate the method. It is shown that the present scheme maintain a first-order spatial accuracy and can simulate flows around stationary and moving solid bodies with accurate non-slip boundary condition. The errors are smaller than those of the existing IB–LB schemes. The present method is also validated by simulating the mechanical heart valve flow. The good agreement with experimental data and better results than other numerical methods demonstrate that our current method has great potential for practical applications.

However, it should be pointed out that although the non-slip boundary condition is satisfied with good accuracy at walls, an interpolation procedure is inevitable and the interpolation precision can be affected by the velocity distribution in the immersed boundary layer and the orientation of the Eulerian mesh to the Lagrangian grid. In this sense, very fine mesh near the boundary is necessary for simulation of flows at high Reynolds numbers.

## Acknowledgements

This work was supported by the National Natural Science Foundation of China (NSFC, Grant Nos. 10572106, 10872153 and 11172219) and the Specialized Research Fund for the Doctoral Program of Higher Education of China (Grant No. 20130141110013).

## References

[1] C.S. Peskin, Flow Patterns Around Heart Valves: A Digital Computer Method for Solving the Equations of Motion, PhD Thesis, *Physiol. Albert Einstein Coll. Med., Univ. Microfilms*, vol. 378, 1972, pp. 72–102.

[2] McQueen DM, Peskin CS. A three-dimensional computer model of the human heart for studying cardiac fluid dynamics. *Comput. Graphics* 2000;34:56–60.

[3] Borazjani I. Fluid–structure interaction, immersed boundary–finite element method simulations of bio-prosthetic heart valves. *Comput. Method. Appl. M* 2003;257:103–16.

[4] Dillon R, Fauci L, Gaver D III. A microscale model of bacterial swimming, chemotaxis and substrate transport. *J. Theor. Biol.* 1995;177:325–40.

[5] Fauci LJ, Peskin CS. A computational model of aquatic animal locomotion. *J. Comput. Phys.* 1988;77:85–108.

[6] Zhang JF, Johnson PC, Popel AS. Red blood cell aggregation and dissociation in shear flows simulated by lattice Boltzmann method. *J. Biomech.* 2008;41:47–55.

[7] Sui Y, Chew YT, Roy P, Low HT. A hybrid method to study flow-induced deformation of three-dimensional capsules. *J. Comput. Phys.* 2008;227:6351–71.

[8] Krüger T, Varnik F, Raabe D. Efficient and accurate simulations of deformable particles immersed in a fluid using a combined immersed boundary lattice Boltzmann finite element method. *Comput. Math. Appl. M* 2011;61:3485–505.

[9] Zhu LD, Peskin CS. Simulation of a flapping flexible filament in a flowing soap film by the immersed boundary method. *J. Comput. Phys.* 2002;179:452–68.

[10] Zhu LD, He GW, Z Wang S, et al. An immersed boundary method based on the lattice Boltzmann approach in three dimensions, with application. *Comput. Math. Appl. M* 2011;61:3506–18.

[11] Kim Y, Peskin CS. 3-D Parachute simulation by the immersed boundary method. *Comput. Fluids* 2009;38:1080–90.

[12] Qian YH, d’Humières D, Lallemand P. Lattice BGK models for Navier–Stokes equation. *Europhys. Lett.* 1992;17:479–84.

[13] Chen HD, Chen SY, Matthaeus WH, et al. Recovery of the Navier–Stokes equations using a lattice-gas Boltzmann method. *Phys. Rev. A* 1992;45:R5339–42.

[14] Chen S, Doolen GD. Lattice Boltzmann method for fluid flows. *Annu. Rev. Fluid. Mech.* 1998;30:329–64.

[15] Tölke J, Krafczyk M. TeraFLOP computing on a desktop PC with GPUs for 3D CFD. *Int. J. Comput. Fluid. D* 2008;22:443–56.

[16] Zheng HW, Shu C, Chew YT. A lattice Boltzmann model for multiphase flows with large density ratio. *J. Comput. Phys.* 2006;218:353–71.

[17] Yu HD, Luo LS, Girimaji SS. LES of turbulent square jet flow using an MRT lattice Boltzmann model. *Comput. Fluids* 2006;35:957–65.

[18] Zhou J. A lattice Boltzmann model for the shallow water equations. *Comput. Math. Appl.* 2002;32:3527–39.

[19] Cheng YG, Zhang H. Immersed boundary method and lattice Boltzmann method coupled FSI simulation of mitral leaflet flow. *Comput. Fluids* 2010;39:871–81.

[20] Tian FB, Luo HX, Zhu LD, Liao JC, et al. An efficient immersed boundary–lattice Boltzmann method for the hydrodynamic interaction of elastic filaments. *J. Comput. Phys.* 2011;230:7266–83.

[21] Hao J, Zhu LD. A lattice Boltzmann based implicit immersed boundary method for fluid–structure interaction. *Comput. Math. Appl.* 2010;59:185–93.

[22] Feng ZG, Michaelides EE. The immersed boundary–lattice Boltzmann method for solving fluid–particles interaction problems. *J. Comput. Phys.* 2004;195:602–28.

[23] Niu XD, Shu C, Chew YT, Peng Y. A momentum exchange-based immersed boundary–lattice Boltzmann method for simulating incompressible viscous flows. *Phys. Lett. A* 2006;354:173–82.

[24] Dupuis A, Chatelain P, Koumoutsakos P. An immersed boundary–lattice Boltzmann method for the simulation of the flow past an impulsively started cylinder. *J. Comput. Phys.* 2008;227:4486–98.

[25] Cheng YG, Zhang H, Liu C. Immersed boundary–lattice Boltzmann coupling scheme for fluid–structure interaction with flexible boundary. *Commun. Comput. Phys.* 2011;9:1375–96.

[26] Wu J, Shu C. Implicit velocity correction-based immersed boundary–lattice Boltzmann method and its applications. *J. Comput. Phys.* 2009;228:1963–79.

[27] Cheng YG, Zhu LZ, Zhang CZ. Numerical study of stability and accuracy of the immersed boundary method coupled to the lattice Boltzmann BGK model. *Commun. Comput. Phys.* 2014;16:136–68.

[28] Guo ZL, Zheng CG, Shi BC. Discrete lattice effects on the forcing term in the lattice. *Phys. Rev. E* 2002;65:46308.

[29] Cheng YG, Li JP. Introducing unsteady non-uniform source terms into the lattice Boltzmann model. *Int. J. Numer. Methods Fluids* 2008;56:629–41.

[30] d’Humières, Ginzburg I, Krafczyk M, Lallemand P, Luo LS. Multiple-relaxation time lattice Boltzmann models in three dimensions. *Philos. Trans. Royal. Soc. A* 2002;360:437–51.

[31] He XY, Luo LS. Lattice Boltzmann model for incompressible Navier–Stokes equation. *J. Stat. Phys.* 1997;88:927–44.

[32] Peng Y, Luo LS. A comparative study of immersed-boundary and interpolated bounce-back methods in LBE. *Prog. Comput. Fluid. Dy.* 2008:156–67.

[33] Luo K, Wang ZL, R Fan J, et al. Full-scale solutions to particle-laden flows: multi-direct forcing and immersed boundary method. *Phys. Rev. E* 2007;76:066709.

[34] williamnson CHK. Vortex dynamic in the cylinder wake. *Annu. Rev. Fluid Mech.* 1996;28:477–539.

[35] Silva ALFLE, Silvera-Neto A, Damasceno JJR. Numerical simulation of two-dimensional flows over a circular cylinder using the immersed boundary method. *J. Comput. Phys.* 2003;189:351–70.

[36] Lai MC, Peskin CS. An immersed boundary method with formal second-order accuracy and reduced numerical viscosity. *J. Comput. Phys.* 2000;160:705–19.

- [37] Su SW, Lai MC, Lin CA. A simple immersed boundary technique for simulating complex flows with rigid boundary. *Comput. Fluids* 2007;36:313–24.
- [38] Le GG, Zhang JF. Boundary slip from the immersed boundary lattice Boltzmann models. *Phys. Rev. E* 2009;79:026701.
- [39] Stijnen JMA, de Hart J, Bovendeerd PHM, et al. Evaluation of a fictitious domain method for predicting dynamic response of mechanical heart valves. *J. Fluids Struct.* 2004;19:835–50.
- [40] Vierendeels J, Dumont K, Dick E. Analysis and stabilization of fluid–structure interaction algorithm for rigid-body motion. *Am. Inst. Aeronaut. Astronaut.* 2005;43:2549–57.
- [41] Dumont K, Stijnen JMA, Vierendeels J, et al. Validation of a fluid–structure interaction model of a heart valve using the dynamic mesh method in fluent. *Comput. Methods Biomed. Eng.* 2004;7:139–46.